Quantitative modeling of spintronic terahertz emission due to ultrafast spin transport

Francesco Foggetti[*] and Peter M. Oppeneer[†]
Department of Physics and Astronomy, Uppsala University, P. O. Box 516, Uppsala SE-751 20, Sweden

(Received 15 November 2024; revised 19 December 2024; accepted 24 December 2024; published 28 January 2025)

In spintronic terahertz (THz) emitters, THz radiation is generated by exciting an ultrafast spin current through femtosecond laser excitation of a ferromagnetic-nonmagnetic metallic heterostructure. Although an extensive phenomenological knowledge has been built up during the last decade, a solid theoretical modeling that connects the generated THz signal to the laser induced-spin current is still incomplete. Here, starting from general solutions to Maxwell's equations, we model the electric field generated by a superdiffusive spin current in spintronic emitters, taking Co/Pt as a typical example. We explicitly include the detector shape, which is shown to significantly influence the detected THz radiation. Additionally, the electron energy dependence of the spin Hall effect is taken into account, as well as the duration of the exciting laser pulse and the thickness of the detector crystal. Our modeling leads to realistic emission profiles and highlights the role of the detection method for distinguishing key features of the spintronic THz emission.

DOI: 10.1103/PhysRevApplied.23.014067

I. INTRODUCTION

The terahertz (THz) region is defined as the interval in the electromagnetic spectrum with frequencies in the range of about 0.3 to 30 THz [1–4]. As the number of possible THz-based applications continues to grow, spanning diverse fields such as imaging, security, communication, and high-speed electronics [2,5,6], the last decade has been characterized by a great effort to realize efficient THz emitters [7–11].

Current state-of-the-art THz emitters are nonlinear semiconductor crystals that emit THz radiation due to optical rectification or, alternatively, photoconductive antennas [3,8,12,13]. However, the limited bandwidth of these emitters has motivated investigations into alternative solid-state emitters. A few years ago, spintronic THz emitters were discovered as a promising class of emitters that could offer a wide bandwidth of 10 THz or more [7,11,14–21].

The general structure of a spintronic THz emitter consists of a bilayer of a ferromagnetic (FM) metal and a nonmagnetic (NM) heavy metal, with layer thicknesses of several nanometers [7,11,15–20]. Despite this simple structure, and although significant experimental studies have been performed, the physical origin of the THz emission continues to be disputed (see, for example, [22]). It has meanwhile become mostly accepted that the laser-induced demagnetization of the FM layer leads to injection of a spin current from the FM layer into the NM heavy-metal layer, where the inverse spin Hall effect (ISHE) leads to the conversion of the spin current to a charge-current pulse which, through electric dipole emission, causes the THz radiation. However, two aspects continue to be debated. The first aspect is the source of the spin current. The spin current has been attributed to several different physical mechanisms, such as the generation of a spin-polarized current of nonthermal electrons in the superdiffusive transport regime [14,23,24], or to the generation of a thermal spin current through the spin Seebeck effect [25–27]. Another recently developed model, called the dM/dt model, attributes the spin current to spin pumping from the FM to the NM layer [28,29]. Also, diffusive spin transport has been used to model the THz emission [17]. Recently, it was furthermore argued that the spin-to-charge conversion in the NM heavy-metal layer does not make an essential contribution to the THz emission [22].

A second debated issue is whether the emitted THz electric field is proportional to the charge current $\mathbf{J}$ or to its time derivative, $\partial\mathbf{J}/\partial t$ (see, for example, Refs. [7,22,30–34]). Obviously, the THz bandwidth depends strongly on whether the THz signal is due to the charge current or its derivative, as the latter will display

[*]Contact author: francesco.foggetti@physics.uu.se, foggettifrancesco@libero.it
[†]Contact author: peter.oppeneer@physics.uu.se

Published by the American Physical Society under the terms of the Creative Commons Attribution 4.0 International license. Further distribution of this work must maintain attribution to the author(s) and the published article's title, journal citation, and DOI. Funded by Bibsam.

a different and stronger time dependence and thus a much wider bandwidth. Taken together, the lack of understanding of the source of the spintronic THz emission, how it is generated and leads to the measured THz electric field hampers the development of efficient spintronic THz emitters as well as the precise extraction of typical spintronic quantities from the THz signal, such as the spin diffusion length [35].

Our aim here is to provide a quantitative theoretical description of spintronic THz emission. We focus first on two aspects behind THz emission: the ultrafast dynamics of electrons in the emitter and the relation between the excited spin current and the generated THz electric field, which is experimentally well reported but not fully justified theoretically [22,32]. There exists namely an inconsistency between the experimental observations and theory based on Maxwell's equations, specifically, Jefimenko's equation [36], which establishes that the emitted electric field should be proportional to the time derivative of the electric current. We solve this issue by taking into account the influence of the experimental setup and show that there is no contradiction, because the detecting system effectively integrates the THz signal in time. Considering a Co(2 nm)/Pt(4 nm) bilayer as a typical spintronic THz emitter [10,15,17,37,38], we then use the superdiffusive (SD) spin transport theory [23,24,39] to describe the inner dynamics of electrons upon ultrafast laser excitation, and specifically show that the dependence of the spin Hall effect on the energy of the laser excited electron plays a role for the bandwidth of the THz emission. We further show that the duration of the excitation pulse strongly affects the detected THz signal. Lastly, we take into account the thickness of the electro-optical detector crystal in the simulations to obtain realistic THz emission profiles.

We first introduce our theoretical modeling of THz emission in Sec. II, followed by computed results for a typical Co/Pt emitter in Sec. III.

II. MODEL

A. THz electric field emission

To describe the electric field $\mathbf{E}(\mathbf{r},t)$ generated in three-dimensional space from the charge current and the time-varying charge densities in the metallic bilayer, we employ Jefimenko's equation [36]

$$\mathbf{E}(\mathbf{r},t) = \frac{1}{4\pi\epsilon_0}\int d\mathbf{r}'\left[\frac{(\mathbf{r}-\mathbf{r}')}{|\mathbf{r}-\mathbf{r}'|^3}\rho(\mathbf{r}',t_r) + \frac{1}{c}\frac{(\mathbf{r}-\mathbf{r}')}{|\mathbf{r}-\mathbf{r}'|^2}\frac{\partial\rho(\mathbf{r}',t_r)}{\partial t} - \frac{1}{c^2}\frac{1}{|\mathbf{r}-\mathbf{r}'|}\frac{\partial\mathbf{J}(\mathbf{r}',t_r)}{\partial t}\right]. \tag{1}$$

In this expression, which is the exact solution of the Maxwell equations, the sources of the THz emission are, respectively, the charge density ρ, its time derivative $\partial\rho/\partial t$, and the time derivative of the charge-current density $\partial\mathbf{J}/\partial t$. The integral runs over the volume of the spintronic emitter, where $\mathbf{r}'$ represents the spatial element inside the emitter and t_r is the retarded time $t_r = t - |\mathbf{r}-\mathbf{r}'|/c$. The retarded time takes into account the change in the source terms happening on timescales comparable to the emission timescales; that is, the speed of excited electrons moving in the spintronic emitter is of the order of nanometers per femtosecond, which is not negligible with respect of the speed of light c (approximately 300 nm/fs). A short derivation of Eq. (1) is given in Appendix A 1.

The three terms in Eq. (1) have different decay properties: when the detector is far away from the system (far-field limit), the sign of the term $\mathbf{r}-\mathbf{r}'$ is well defined, and so the first term decays as inverse of the square of the distance while the second and third decay simply as the inverse of the distance. In Appendix A 2 we discuss how the contribution of the second term is zero due to conservation of charge, while the first term, by using the continuity equation $\partial\rho/\partial t + \nabla\cdot\mathbf{J} = 0$, becomes proportional to the current density. Comparing the decay properties, the third term, which decays as the inverse of the distance, will contribute the most in the far field. This observation is consistent with the THz electric field being proportional to $\partial\mathbf{J}/\partial t$, as has been stated in several recent investigations [22,32–34].

A few summarizing comments are appropriate at this point. Jefimenko's equation gives two contributions, a near-field contribution, the first term in Eq. (1), for which the THz field is proportional to the charge current $\mathbf{J}$ (as we show in Appendix A 2), and a far-field contribution proportional to $\partial\mathbf{J}/\partial t$. This is consistent with previous work by Kaplan [40], who solved the paraxial wave equation and found that, in the far-field limit, the traveling pulse becomes proportional to its time derivative.

On the other hand, several experimental works [7,30,31] used a different method to estimate the emitted THz field. In these works, a common element is the use of a one-dimensional wave equation to compute the electric field at the NM-vacuum interface. As a result, they obtain a current-proportional field, $\mathbf{E}\propto\mathbf{J}$. This solution does not depend on the distance from the emitter, which is due to the choice of solving the wave equation in one dimension; that is to say, one obtains a solution that does not decay in space. However, Jefimenko's equation gives that, far from the source, in three dimensions the electric field decays proportionally to the inverse of the distance, consistent with energy conservation. But in one dimension, there is no geometrical dilution of the emitted energy and, as such, the emitted wave does not decay with the distance. For this reason, the solution proposed in the above works is incomplete, and we consider our approach based on the Jefimenko's equation, which is a solution in the whole space, more general.

B. Influence of detector on THz signal

To address the issue of the proportionality of the THz signal, we now consider the influence of the presence of a macroscopic detector on the shape of the detected THz signal. In the measurements, the radiation emitted from the sample is propagated through the experimental setup and collected into the detector with the use of several parabolic mirrors. The presence of these mirrors, especially if not perfectly aligned, could introduce delays or distortions in the collected signal; however, the following conclusions hold true independently of other optical elements besides the last mirror. Thus, we can consider the last mirror, the one that focuses the radiation onto the detector, effectively as a macroscopic emitter where every point of the mirror can be considered as an emission center. When a nonpointlike source emits a signal, the signal emitted from every different point reaches the detector at different times. As a result the signal is effectively integrated in time, as sketched in Fig. 1(a), resulting in an electric field which is proportional to the current in the spintronic device, as outlined below. Figure 1(b) gives an intuitive picture of how the reflected radiation from every point of the mirror would reach the detector with a time delay due to the position of the different points of the mirror.

The detected electric field can thus be obtained by considering the far-field term in Eq. (1) and integrating it over the surface of the mirror

$$\mathbf{E}(t) \propto \int d\mathbf{s}\, \frac{\partial \mathbf{J}}{\partial t}(t_r)\,, \tag{2}$$

where $d\mathbf{s}$ is the element of surface area. The time dependence of the current with respect of the emission point is contained in the retarded time t_r, where the distance from the focal point of the mirror (where the detector is located) causes different points on the mirror to correspond to different values of t_r. The straightforward relation between the space and time coordinates allows us to rewrite the integral in Eq. (2) as an integral over dt; for technical details, see Appendix B 1. Explicit numerical integration over the mirror surface and comparing $\mathbf{E}(t)$ with the charge current $\mathbf{J}(t)$ gives that their shapes are practically identical. Therefore, after the integration, the measured time-dependent electric field is proportional to the charge current, $\mathbf{E}(t) \propto \mathbf{J}(t)$, even in the far field. The solution to the apparent contradiction of an emitted electric field proportional to the current derivative or the current itself lies thus in the way the emitted field is collected into the detector.

It should additionally be mentioned that, for the detection scheme examined, the parabolic mirrors used to collect the radiation into the detector are off-axis parabolic mirrors. These mirrors are obtained as a section of a three-dimensional paraboloid, so that the radiation is incident on the mirror and is reflected into the detector at an angle. In the above, we considered for simplicity a *centered* mirror, where the direction of incident and reflected radiation is parallel to the optical axis of the mirror. This would obviously not be a suitable experimental setup, as the detector would screen the mirror from the radiation emitted by the device, hence the need for off-axis mirrors. A longer derivation given in Appendix B shows that this approximation does not change the results qualitatively.

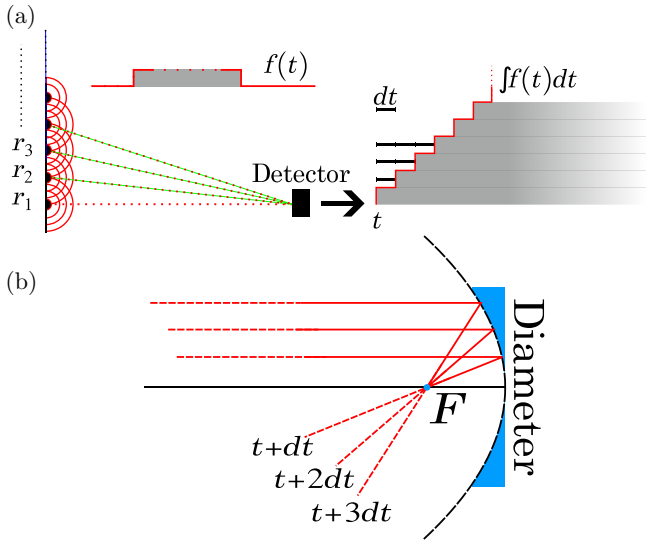

FIG. 1. Schematic representation of the integration of the THz signal over a surface. (a) As the signal $f(t)$ is emitted from multiple source points r_i, these signals reach the detector at different times, where they are summed with a time delay proportional to dt, resulting in a time integration of the signal. (b) Focusing of the signal by the parabolic mirror: every point of the mirror acts as an emission point, and the signal reaches the focal point F at a different time for every emission point.

C. The superdiffusive spin-transport model

We use here the SD spin-transport theory [23,24,39,41] to model the laser-induced ultrafast spin current in a selected FM/NM system. The laser pulse excites spin-up and spin-down electrons in the FM layer of the spintronic emitter and, since the two spin channels have different transport properties (i.e., different velocities and lifetimes of electrons), the excited current that is injected from the FM to the NM layer is spin polarized. The spin current flux into the NM is the amount of demagnetization of the FM layer, $\partial M/\partial t$. The demagnetization due to fast optically induced spin injection is hence considered here as a longitudinal magnetization reduction. It does not include transversal spin precession, which can lead to spin pumping on longer timescales.

The spintronic emitter is described as a quasi-one-dimensional system in the z direction, normal to the heterostructure. This approximation is justified by the

nanometer thickness of the emitter, compared to the micrometer-size spot of the pump laser. The density of excited electrons $n_\sigma(\epsilon, z, t)$, with σ being the electron spin, ϵ its energy and (z, t) the space and time coordinates, is described by the transport equation [23,24,39]

$$\frac{\partial n_\sigma}{\partial t} + \frac{n_\sigma}{\tau_\sigma} = \left(-\frac{\partial}{\partial t}\hat{\phi} + \hat{I}\right) S_\sigma^{\text{eff}}, \tag{3}$$

where, for simplicity, we omitted the dependence on the variables (ϵ, z, t). Here, $\tau_\sigma = \tau_\sigma(\epsilon, z)$ is a hot electron lifetime that depends on the energy and spin of electrons and the material we consider. The operator $\hat{\phi}$ describes the electron flux in the system, and contains information about scattering events, interactions among electrons, between electrons and the lattice, spin flip, lifetime and velocities of the electrons. Note that although Eq. (3) is quasi-one-dimensional, it is derived from the full three-dimensional spin flux by statistically averaging over the spherical angles; see [24]. The term $\hat{I}$ is the identity operator, while S_σ^{eff} represents the effective spin source, consisting of both the contributions from the laser-excited electrons S_σ^{ext}, modeled as a Gaussian shaped pulse, and those excited through scattering events S_σ^{p} so that $S_\sigma^{\text{eff}} = S_\sigma^{\text{ext}} + S_\sigma^{\text{p}}$. We solve Eq. (3) numerically for the true geometry of the sample and take the time duration of the laser pulse into account. Doing so for a chosen heterostructure, we obtain the time-dependent nonthermal electron density $n_\sigma(\epsilon, z, t)$ and the spin-current density $j_s(z, t)$ from which we numerically compute the charge current and resulting THz emission.

The SD spin transport theory is a material-specific theory through the hot electron lifetimes and velocities. We therefore consider specifically a Co(2 nm)/Pt(4 nm) system as representative of a typical THz emitter [10,15,17,37,38]. The spin-dependent hot electron lifetimes and velocities are taken from first-principles calculations [42,43]. Furthermore, we assume excitation of the THz layer by a 1.5-eV pump laser, as used in most experiments, and investigate the influence of the pump pulse duration in Sec. III.

D. Spin-to-charge conversion

When the spin current is injected in the NM layer, it is converted via the ISHE [14,44,45] into a transient charge current as $J_c(z, t) = 2e/(\hbar)\theta_{\text{SH}} J_s(z, t)$, where θ_{SH} is the spin Hall angle. θ_{SH} is defined in terms of the spin Hall conductivity σ_{SH} and the normal electrical conductivity σ_e as $\theta_{\text{SH}} = 2\sigma_{\text{SH}}/\sigma_{\text{e}}$ and it represents the efficiency of the spin-to-charge conversion process.

The rate of spin-to-charge conversion depends on θ_{SH} and, hence, on the spin Hall conductivity, which is a quantity that is usually electron-energy dependent [46]. In our simulations, the NM material is Pt, which has a strong energy-dependent spin Hall conductivity [46]. In particular, σ_{SH} for Pt is large for electrons close to the Fermi level, but it decreases significantly for energies higher than 0.5 eV, meaning that excited electrons with energy higher than this value will give negligible contributions to the charge current. However, high-energy electrons can still contribute to the emission via scattering processes. When electrons scatter, they lose energy and decay into lower energy levels and populate the energy channels, which can make significant contributions to the THz emission.

To include the energy dependence of the spin-charge conversion we proceed as follows. When solving Eq. (3) numerically we obtain the energy-dependent electron density $n_\sigma(\epsilon, z, t)$, where the energy ϵ assumes values from 0 to 1.5 eV in 12 discrete energy levels. As only the levels of energy not higher than 0.5 eV contribute to the emission, only the first three energy levels can efficiently be converted into a charge current through the ISHE. We suppose that every electron can decay from its energy level to the energy below with a decay time of τ_ϵ. For simplicity, we do not consider the case where electrons can decay multiple levels at once, but must go through all the intermediate levels if they decay into a level which is not immediately below in energy. Additionally, we assume that spin is conserved in the decay, that is, no spin flip happens while the electron loses energy. Therefore, after the decay, the new electron density n_{dec} is described by the equation

$$n_{\text{dec}}(\epsilon, t+\delta t) = \Big[n(\epsilon, t+\delta t) + n_{\text{dec}}(\epsilon+1, t+\delta t) + e^{-\frac{\delta t}{\tau_\epsilon}}\left(n(\epsilon, t) + n_{\text{dec}}(\epsilon+1, t)\right)\Big]\left(1 - e^{-\frac{\delta t}{\tau_\epsilon}}\right), \tag{4}$$

where the spin index has been omitted for the sake of simplicity.

We point out that, for every energy level, n_{dec} is composed of contributions from the original excited density n (electrons of that level that did not decay) and from the electrons that decayed from higher-lying energy levels. Finally, we use the three lowest energy levels of the new computed electron density to compute numerically the charge current that will then give rise to the THz emission.

Figure 2 shows the influence of the energy dependence of the spin-to-charge conversion due to the ISHE on the computed charge current, for the Co(2 nm)/Pt(4 nm) bilayer excited with a 20-fs laser pulse. We note that, if the spin Hall angle is kept uniform in the 0–1.5-eV range, then the charge current would simply be proportional to the spin current which, in the superdiffusion theory, is computed through the spin flux in the sample [23,24,41]. However, when using an energy-dependent spin Hall angle, the exact proportionality between charge current and spin current is lost. In particular, we compute the charge current by using the continuity equation in conjunction with the new electron density n_{dec} computed in Eq. (4), restricted to the lower energy levels. This results in the change in the

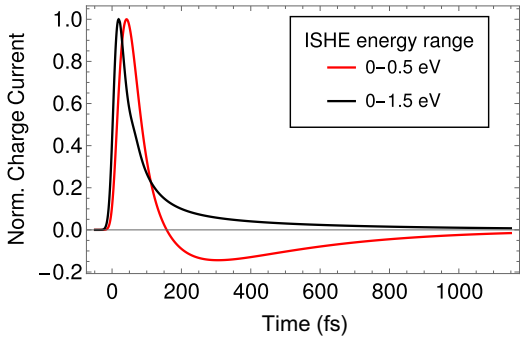

FIG. 2. Influence of the energy dependence of the ISHE on the transient charge current. The black line gives the computed charge signal when all excited electrons contribute to the spin-charge conversion, and the red curve when only the spin-polarized hot electrons with energies up to 0.5 eV contribute. A pump pulse of 20 fs was used in the calculations.

shape of the charge current with respect to the spin current shown in Fig. 2. Moreover, the charge current pulse peaks at a later time, as expected, since excited spin-majority electrons need to decay to lower energy levels to contribute to the charge current. In addition, the influence of later arriving spin-minority electrons becomes more pronounced.

III. RESULTS

A. Detector orientation

We start by comparing the charge current in the Co/Pt spintronic device with the collected THz electric field for different mirror configurations, assuming a 20-fs laser pulse. We consider here three cases: a centered mirror, a 15°, and a 45° off-axis parabolic mirror, where the angle refers to the angle between the incident radiation and the optical axis of the mirror, that is, the axis that connects the center of the mirror with the focus of the parabola; see Appendix B 2 for details. All the mirrors have a diameter of 50 mm and a focal distance of 100 mm.

Figure 3(a) shows the comparison between the transient charge-current profile in the Co/Pt spintronic device (black dashed line) with the collected electric field signal for the mirrors considered. We can see that, after employing Jefimenko's Eq. (1) to obtain the far field $E(t)$, the integration over the centered mirror (green line) perfectly superimposes with the current profile from the emitter. Thus, the focusing mirror effectively converts the THz signal proportional to $\partial J/\partial t$, to an $E(t) \propto J(t)$ signal. For the off-axis mirrors, we see that the integration over the 15° mirror produces a signal really similar to the original current profile, with a slight stretch of the profile in time, while the 45° mirror induces a significantly larger time stretch.

The mirror configuration has interesting effects on the measured bandwidth, too. Figure 3(b) shows, in Fourier space, the resulting electric field as computed from the

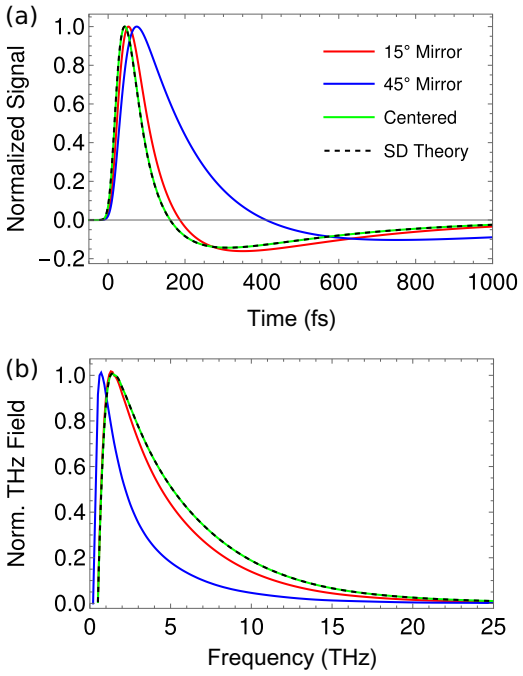

FIG. 3. Influence of detector mirror on the THz signal of the Co/Pt emitter. (a) Transient THz electric field after the integration over the surface of the mirror for 15° (red), 45° (blue) off-axis and centered (green curve) mirrors compared with the charge current obtained from the superdiffusive (SD) model (dashed black curve). (b) Bandwidth of the THz signals obtained after integrating over the surface of the mirror (same color legend as under (a)), compared with the bandwidth obtained from the calculated charge current (dashed black line). The curves have been normalized to the same peak value for easier visualization.

original current and from the THz signal that has been integrated over the surface of the mirrors. As for the previous case, the signal integrated on the centered mirror provides an exact superposition with the profile of the original current, while the 15° signal appears to be slightly reduced in bandwidth and the signal for the 45° mirror has a bandwidth that is more reduced with respect to that from the original source.

B. Simulated THz bandwidth

We now consider the influence of the laser pulse duration and of the electro-optical sampling with a nonlinear ZnTe crystal. Figure 4 shows the computed THz bandwidth for the Co(2 nm)/Pt(4 nm) system. For comparison, we show the THz bandwidths computed for the E field proportional to the current or to the current derivative. For sake of simplicity, we consider the case of a centered mirror. The received THz signal is then exactly proportional to the charge current and not distorted as shown in Fig. 3, so that a direct comparison with the current-derivative signal, computed in absence of mirrors (and hence not distorted), is straightforward.

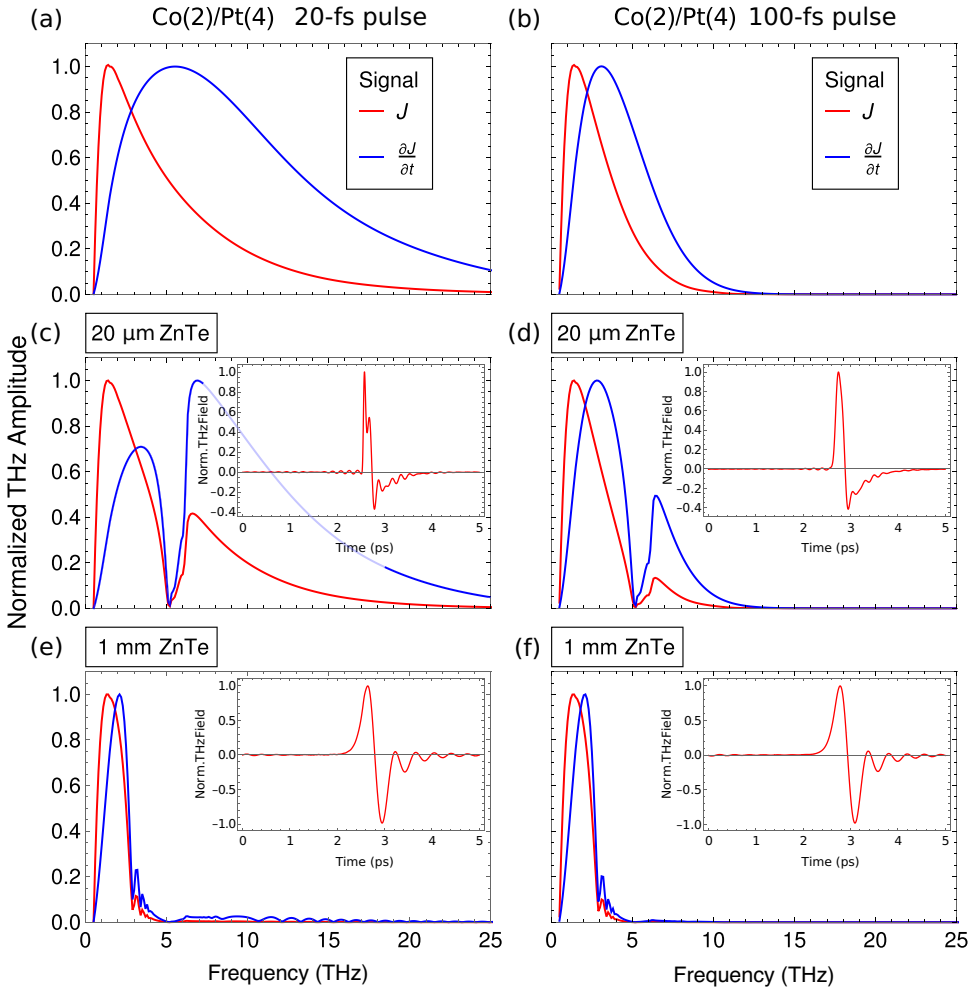

FIG. 4. Spintronic THz spectra computed for a Co/Pt emitter. The THz bandwidth generated from the charge current (red) and the charge-current derivative (blue) are compared for short (left panels) and long (right panels) pump laser pulses. (a) Simulated signals generated by the charge-current derivative and by the charge current for a 20-fs laser pulse, and (b) for a 100-fs long pump pulse. (c),(d) Simulated THz signals convoluted with the response function of a 20-μm-thick ZnTe electro-optical crystal for (c) short and (d) long pulses. (e),(f) Simulated THz signals convoluted with the response function of a 1-mm-thick ZnTe crystal for (e) short and (f) long pulses. The insets in panels (c)–(f) show the time trace of the THz electric field generated by the charge current J.

Furthermore, we take into account the effects of different exciting laser pulse lengths (1.5 eV, 20 fs and 100 fs) as well as the response function of a ZnTe crystal commonly used for the THz detection [47–49]. A number of very interesting observations can be extracted from our results.

First, let us consider only the predicted THz emission profile, without taking into account the response function of the detecting crystal, in Figs. 4(a) and 4(b). For short exciting laser pulses, the difference between the THz signal induced by the current and that induced by the current derivative is striking; $E \propto \partial J/\partial t$ results in a very broad emission, of the order of 30 THz, while $E \propto J$ gives a much narrower emission, of the order of 5–10 THz. However, when laser pulses with longer pulse width (approximately 100 fs) are used to excite the system, the differences between the two emission profiles appear much less pronounced, with a more similar bandwidth. Therefore, when comparing THz signals, particular attention must be paid to the pulse width used, since long exciting pulses would make it particularly challenging to distinguish the two emission mechanisms.

Second, the response function of the detection crystal plays a fundamental role in the detection. Figures 4(c) and 4(d) show the predicted THz emission profiles convoluted with the response function of a ZnTe crystal [47]; see Appendix C for details regarding the derivation of the response function. We consider two cases, a thin (20 μm) and thick (1 mm) ZnTe crystal. The use of a crystal of

a certain thickness introduces an additional filter to the detected THz frequency spectrum. If the crystal is thin enough, the detected spectrum is not considerably reduced, as we can see in the case of the 20 μm crystal: aside from a sharp dip at approximately 5 THz, the detected bandwidth is still large enough so that emission profiles due to the charge current or its derivative can be distinguished.

For short exciting pulses (20 fs) the $E \propto J$ and $E \propto \partial J/\partial t$ signals are remarkably different, but this difference is less evident for long pump pulses. The case of the thick electro-optical crystal is also very interesting. As the thickness of the crystal increases, the frequency window of the detector is dramatically reduced (see Appendix Fig. 7), therefore reducing both the signal computed from the current and the current derivative, for both short and long excitation pulses, leading to THz spectra being almost indistinguishable in practice.

The insets in Figs. 4(c)–4(f) show the time-domain electric signal due to the charge current J and include the influence of the thickness of the ZnTe crystal. The THz time traces exhibit a characteristic bipolar shape comparable to THz pulses observed in experiments [10,17,21,25,37]. Analogous to the observations made for the THz bandwidth, the time traces for long and short pump pulses are practically indistinguishable when a 1-mm-thick electro-optical crystal is used for detection.

IV. DISCUSSION AND CONCLUSIONS

Several aspects of spintronic THz emission have recently been debated. First, the source of the emission has been disputed. Magnetic dipole emission due to a rapid change of magnetization ($E \propto \partial^2 M/\partial t^2$) was first proposed as source of THz emission [50]. Such a source of THz emission could occur in single thin ferromagnetic films, but it has been shown that in FM/NM bilayers the electric dipole emission is responsible for the much stronger THz emission and, moreover, consistent with spin-charge conversion due to the ISHE [14,51]. Second, different proportionalities of the emitted THz field have been proposed, being proportional to either the charge current or the time derivative of the charge current [7,22,25,32–34]. The lack of agreement between experimental and theoretical works has hindered the process of supporting experiments with a suitable theoretical framework, as well as precluding the testing of different theoretical models through experimental verification, thus slowing down the advancement in the field. We find that, although the proportionality to $\partial J/\partial t$ is consistent with Maxwell theory, investigating the influence of the parabolic mirror shows that this detection method effectively leads to a time integration of the signal, making it proportional to the charge current. The measured far-field THz signal then acquires a current-field proportionality, which is similar to the proportionality obtained from a one-dimensional wave equation [30,31], but obviously for entirely different reasons. It deserves to be mentioned, too, that apart from the ISHE, operative in the bulk metallic NM layer, THz emission due to a local spin-charge conversion as the inverse Rashba-Edelstein effect was proposed for systems with a Rashba surface state, such as an FM layer covered with a thin Ag/Bi layer [52,53], or with ultrathin $Bi_{1+x}Sb_x$ [54].

We further find that the experimental configuration (detector crystal and mirror configuration) as well as the duration of the laser pump can affect the profile of the recorded THz signal substantially. In essence, we obtain that, when the exciting pulses are relatively long (50–100 fs) or the detector crystal is quite thick (approximately 1 mm), the THz bandwidth becomes reduced. The emitted THz spectra for the two cases ($E \propto J$ or $\propto \partial J/\partial t$) are then hardly distinguishable. This may provide an explanation for why the debate between current and current-derivative THz emission has not yet reached a conclusion. We further conclude from our simulations that, to distinguish clearly between a current and a current-derivative THz signal, thin electro-optic crystals, less than 50 μm, should be used for detection in combination with short pump laser pulses, of the order of 20 fs.

Lastly, the origin of the spin current generated by the pump laser pulse has been debated [14,22,25–29,32]. The different proposed mechanisms for spin current generation, such as, superdiffusion [23,24,39], spin Seebeck effect [25–27], and spin current due to demagnetization [28,29], could be difficult to distinguish in practice. In superdiffusion, the excited spin-polarized electrons are nonthermal, whereas in the spin Seebeck effect and in spin pumping the electrons are considered to have thermalized. Optically induced SD spin currents have been detected in various metallic heterostructures [55–58], but, in early measurements of spintronic THz emission it appeared that the SD spin current was faster than the measured charge current [14]. Taking the integrating effect of the collecting mirror into account, however, quantitative modeling of the THz signal with bandwidths that are overall in agreement with measurements is obtained. Also, as pointed out in Sec. II D, the spin Hall effect has often been assumed to be independent of the electron energy, but a more precise description can be obtained when its energy dependence is included.

Our investigation particularly emphasizes that to explain measured THz emission, several processes need to be modeled, ranging from the real-time excitation and injection of nonequilibrium spin-polarized electrons to their decay due to scattering, spin-charge conversion by an energy-dependent ISHE, and simultaneously occurring electric dipole emission, to the influence of the detection setup on the far-field electric signal. Taking these into account a quantitative explanation of spintronic THz emission can be achieved.

ACKNOWLEDGMENTS

We thank Branislav Nicolić, Tobias Kampfrath, Henri Jaffrès, Francesco Cosco, and Hjalmar Lindstedt for helpful discussions. This work has been supported by the Swedish Research Council (VR), the German Research Foundation (Deutsche Forschungsgemeinschaft) through CRC/TRR 227 "Ultrafast Spin Dynamics" (project MF, project-ID: 328545488)), the K. and A. Wallenberg Foundation (Grants No. 2022.0079 and No. 2023.0336), and the European Union's Horizon 2020 Research and Innovation Programme under FET-OPEN Grant Agreement No. 863155 (s-Nebula). The computational resources were provided by the National Academic Infrastructure for Supercomputing in Sweden (NAISS) at NSC Linköping, partially funded by VR through Grant Agreement No. 2022-06725.

APPENDIX A: ELECTRIC FIELD AS A FUNCTION OF ITS SOURCES

1. Jefimenko's equation for the electric field

Here we provide a brief derivation of the electric field $\mathbf{E}(\mathbf{r},t)$ in terms of its sources, the charge-current density $\mathbf{J}$ and the charge density ρ. To this end, we consider the retarded potentials

$$\phi(\mathbf{r},t) = \frac{1}{4\pi\epsilon_0}\int d\mathbf{r}'\,\frac{\rho(\mathbf{r}',t_r)}{|\mathbf{r}-\mathbf{r}'|} \quad \text{and}$$
$$\mathbf{A}(\mathbf{r},t) = \frac{\mu_0}{4\pi}\int d\mathbf{r}'\,\frac{\mathbf{J}(\mathbf{r}',t_r)}{|\mathbf{r}-\mathbf{r}'|}, \tag{A1}$$

where $\mathbf{r}'$ represents the coordinate inside the domain of integration, $d\mathbf{r}'$ is the volume element, and $t_r = t - |\mathbf{r}-\mathbf{r}'|/c$ is the retarded time. By substituting the expressions for the potentials in the general expression for the electric field, $\mathbf{E}(\mathbf{r},t) = -\nabla\phi(\mathbf{r},t) - \partial\mathbf{A}(\mathbf{r},t)/\partial t$, we obtain

$$\begin{aligned}\mathbf{E}(\mathbf{r},t) &= -\nabla\left(\frac{1}{4\pi\epsilon_0}\int d\mathbf{r}'\,\frac{\rho(\mathbf{r}',t_r)}{|\mathbf{r}-\mathbf{r}'|}\right) - \frac{\partial}{\partial t}\left(\frac{\mu_0}{4\pi}\int d\mathbf{r}'\,\frac{\mathbf{J}(\mathbf{r}',t_r)}{|\mathbf{r}-\mathbf{r}'|}\right)\\ &= \frac{1}{4\pi\epsilon_0}\left[-\nabla\int d\mathbf{r}'\,\frac{\rho(\mathbf{r}',t_r)}{|\mathbf{r}-\mathbf{r}'|} - \mu_0\epsilon_0\frac{\partial}{\partial t}\int d\mathbf{r}'\,\frac{\mathbf{J}(\mathbf{r}',t_r)}{|\mathbf{r}-\mathbf{r}'|}\right].\end{aligned} \tag{A2}$$

Note that $\nabla = \nabla_{\mathbf{r}}$ and both ρ and $\mathbf{J}$ depend on $\mathbf{r}$ implicitly through t_r, and also $\partial/\partial t = \partial/\partial t_r$, so that

$$\nabla\rho(\mathbf{r}',t_r) = \frac{\partial\rho}{\partial t_r}\frac{\partial t_r}{\partial\mathbf{r}} = \left(-\frac{1}{c}\frac{(\mathbf{r}-\mathbf{r}')}{|\mathbf{r}-\mathbf{r}'|}\right)\frac{\partial\rho}{\partial t_r} \quad \text{and} \quad \nabla\left(\frac{1}{|\mathbf{r}-\mathbf{r}'|}\right)\rho = -\frac{(\mathbf{r}-\mathbf{r}')}{|\mathbf{r}-\mathbf{r}'|}\rho, \tag{A3}$$

and this leads to

$$\mathbf{E}(\mathbf{r},t) = \frac{1}{4\pi\epsilon_0}\int d\mathbf{r}'\left[\frac{(\mathbf{r}-\mathbf{r}')}{|\mathbf{r}-\mathbf{r}'|^3}\rho(\mathbf{r}',t_r) + \frac{1}{c}\frac{(\mathbf{r}-\mathbf{r}')}{|\mathbf{r}-\mathbf{r}'|^2}\frac{\partial\rho(\mathbf{r}',t_r)}{\partial t} - \frac{1}{c^2}\frac{1}{|\mathbf{r}-\mathbf{r}'|}\frac{\partial\mathbf{J}(\mathbf{r}',t_r)}{\partial t}\right], \tag{A4}$$

which is the well-known Jefimenko equation for the generated electric field [36].

2. Contributions from Jefimenko's equation

The last two terms of Eq. (A4) decay as the inverse of the distance $|\mathbf{r}-\mathbf{r}'|$, thus they could be detected experimentally at long distances. The last term has already been discussed in the main text, so we focus our attention to the second one.

We show here that the contribution of the second term to the measured electric field, in the system described in the main text, is zero. First, we point out that the vectors $\mathbf{r}$ and $\mathbf{r}'$ represent, respectively, the position of the observer (detector) and the position of the emission center in the sample. As the distance between the detector and the sample is at least of the order of tens of centimeters, and as the dimensions of the emitter vary from the micrometer to the millimeter range, we can safely approximate $\mathbf{r}-\mathbf{r}'$ as $\mathbf{r}$. So the contribution from the second term to the electric field, denoted by $\mathbf{E}^{(2)}$, becomes

$$\mathbf{E}^{(2)}(\mathbf{r},t) \approx \frac{1}{4\pi\epsilon_0}\frac{1}{c}\frac{\hat{\mathbf{r}}}{r}\int d\mathbf{r}'\frac{\partial\rho(\mathbf{r}',t_r)}{\partial t}, \tag{A5}$$

where $\hat{\mathbf{r}}$ is the unit vector in the direction of $\mathbf{r}$. The integral in Eq. (A5) is a volume integral of the time derivative of a charge density, that is, it represents the total flux of charges in or out of the volume of integration. As there are no sources of charge or any sink, the charge is conserved

in the sample, thus the integral in Eq. (A5) must be zero, and the only far-field term contributing to the electric field is the third one, as mentioned in the main text.

For the sake of completeness, we also study the behavior of the first term in Eq. (A4), which decays as the square of the distance. Here we show that it can be expressed in terms of the current density **J**. Using the continuity equation, $\partial\rho/\partial t + \nabla \cdot \mathbf{J} = 0$, we can rewrite the first term of Jefimenko's equation as

$$\frac{1}{4\pi\epsilon_0}\int d\mathbf{r}' \frac{(\mathbf{r}-\mathbf{r}')}{|\mathbf{r}-\mathbf{r}'|^3}\,\rho(\mathbf{r}',t_r) \approx \frac{1}{4\pi\epsilon_0}\frac{\hat{\mathbf{r}}}{r^2}\int d\mathbf{r}'dt\nabla\cdot\mathbf{J}(\mathbf{r}',t_r). \tag{A6}$$

We now focus on the volume integral. We consider a cuboid of dimensions $(\Delta x, \Delta y, \Delta z)$ as the volume of integration that represents our sample and we use the flux theorem to compute the integral. As **J** is not uniform through the volume of integration, the integral is the sum of the fluxes of **J** at every element z' (for simplicity we consider **J** uniform along $\hat{\mathbf{x}}$ and we neglect the x-dependence in the following),

$$\int d\mathbf{r}'\nabla\cdot\mathbf{J}(\mathbf{r}',t_r) = \sum_{z'} S_y^{z'}\left[\mathbf{J}(y_f,z',t_r) - \mathbf{J}(y_i,z',t_r)\right]. \tag{A7}$$

y_f and y_i are the integration boundaries along $\hat{\mathbf{y}}$ and $S_y^{z'}$ is the surface of the cuboid at the element z' that is perpendicular to the current density **J**. If the dimension Δy of the volume of integration is sufficiently small, we can rewrite the previous equation in terms of the y-derivative of **J**,

$$\int d\mathbf{r}'\nabla\cdot\mathbf{J}(\mathbf{r}',t_r) = \sum_{z'} S_y^{z'}\Delta y\frac{\partial\mathbf{J}(y,z',t_r)}{\partial y}. \tag{A8}$$

Additionally, we can rewrite the y-derivative in terms of the time derivative,

$$\frac{\partial}{\partial y} = \frac{\partial}{\partial t}\frac{\partial t}{\partial y} = \frac{1}{v_e}\frac{\partial}{\partial t}, \tag{A9}$$

with v_e the electron velocity in the material. Although electrons of different energies have different velocities, it is straightforward to generalize the equation above to the case of electrons of different velocities, but we omit it here for the sake of brevity. We can now write

$$\int d\mathbf{r}'\nabla\cdot\mathbf{J}(\mathbf{r}',t_r) = \frac{\Delta y}{v_e}\sum_{z'} S_y^{z'}\frac{\partial\mathbf{J}(z',t_r)}{\partial t}, \tag{A10}$$

where for simplicity we removed the dependence on y. Finally, we can sum over z', rewriting Eq. (A6) as

$$\frac{1}{4\pi\epsilon_0}\int d\mathbf{r}' \frac{(\mathbf{r}-\mathbf{r}')}{|\mathbf{r}-\mathbf{r}'|^3}\,\rho(\mathbf{r}',t_r) \approx \frac{1}{4\pi\epsilon_0}\frac{\hat{\mathbf{r}}}{r^2}\frac{\Delta V}{v_e}\mathbf{J}(t_r) \tag{A11}$$

where Δy and the sum over z' of $S_y^{z'}$ have been included in ΔV, and the time derivative of the current has been integrated with respect to time.

To summarize, we showed that the second term of Jefimenko's equation, which is a far-field term, does not contribute to the observed signal due to conservation of charge, while the first term is directly proportional to the current density but is a near-field term, and hence decays much faster than the far-field terms.

APPENDIX B: INTEGRATION OVER THE SURFACE OF THE MIRROR

1. Centered mirror

Here, we integrate the far-field term of Jefimenko's equation over the surface of a parabolic mirror to reproduce the detected THz signal.

In a realistic setup, a number of mirrors and other optic elements are used to redirect and focus the radiation on the detector, and only the last mirror focuses the radiation on it. In the following derivation we consider only the last mirror, and we assume that the experimental setup focuses and redirects the radiation in such a way that it can be considered as a packet of many collinear beams that are all incident on the parabolic mirror with the same angle with respect to the symmetry axis of the mirror.

For simplicity, we first consider the case of a centered mirror, where the emitted beams are parallel to the symmetry axis of the mirror. The expression for the THz electric field emitted due to the current at the position $\mathbf{r}'$ and measured at position **r** and time t is

$$\mathbf{E}(\mathbf{r},t) \approx \int d\mathbf{r}'\frac{1}{|\mathbf{r}-\mathbf{r}'|}\frac{\partial\mathbf{J}}{\partial t}(\mathbf{r}',t_r). \tag{B1}$$

As the radiation emitted from the sample is reflected, we can consider the mirror as the new emitting system and integrate over the surface of the mirror to obtain the signal that is collected into the detector.

In computing the surface integral, we define **r** as the position of the focus of the parabola, and $\mathbf{r}'$ as the generic point on the surface of the mirror. The current density depends on $\mathbf{r}'$ only through the retarded time t_r. As $|\mathbf{r}| \gg |\mathbf{r}'|$, and as the integral is only computed on the surface of the mirror, we can write

$$\mathbf{E}(\mathbf{r},t) \approx \frac{1}{r}\int d\mathbf{s}\frac{\partial\mathbf{J}}{\partial t}(t_r). \tag{B2}$$

We use polar coordinates (ρ,θ) to take advantage of the geometry of the parabolic mirror. F being the focal distance of the parabola, we can rewrite the term $|\mathbf{r}-\mathbf{r}'|$ in

the expression of t_r as $|\mathbf{r}-\mathbf{r}'| = F + \rho^2/4F$, resulting in

$$\mathbf{E}(\mathbf{r},t) \approx \frac{1}{r}\int_0^{2\pi} d\theta \int_0^{\bar{\rho}} d\rho\, \rho \frac{\partial \mathbf{J}}{\partial t}\Big(t - \frac{1}{c}\left(F + \rho^2/4F\right)\Big). \tag{B3}$$

$\mathbf{J}$ does not depend on θ, so we can integrate out the angular variable; $\bar{\rho}$ is the radius of the mirror. Moreover, $\mathbf{J}$ is a smooth function of t, so the derivative can be taken out of the integral, and we change variable, defining $\xi = t - 1/c(F + \rho^2/4F)$ so that

$$\begin{aligned}\mathbf{E}(\mathbf{r},t) &\approx \frac{2\pi}{r}\frac{\partial}{\partial t}\int_{\xi_{\min}}^{\xi_{\max}} d\xi\, 2cF\mathbf{J}(\xi) \\ &= \frac{4\pi cF}{r}\frac{\partial}{\partial t}\Big[\vec{\mathcal{J}}(\xi_{\max}) - \vec{\mathcal{J}}(\xi_{\min})\Big],\end{aligned} \tag{B4}$$

with $\xi_{\max} = \xi(\bar{\rho})$ and $\xi_{\min} = \xi(0)$ and $\partial\vec{\mathcal{J}}/\partial t = \mathbf{J}(t)$. Going back to the original variables, we obtain

$$\mathbf{E}(\mathbf{r},t) \approx \frac{4\pi cF}{r}\left\{\mathbf{J}\Big(t - \frac{1}{c}\Big(\frac{4F^2+\bar{\rho}^2}{4F}\Big)\Big) - \mathbf{J}\Big(t - \frac{F}{c}\Big)\right\}, \tag{B5}$$

which we can rewrite as

$$\mathbf{E}(\mathbf{r},t) \approx -\frac{4\pi cF}{r}\left[\mathbf{J}\left(t\right) - \mathbf{J}\left(t - T\right)\right]. \tag{B6}$$

Due to the integrating effect of the detector mirror the THz signal becomes proportional to the current $\mathbf{J}(t)$, similar to the initial pulse emitted at near field (A11). However, we also notice a change in sign of the signal with respect to the initial pulse; this is consistent with the previously reported Gouy phase shift for THz emission [59,60]. A secondary, backtraveling, and opposite in sign, repetition of the signal appears with a time delay $T = \bar{\rho}^2/4F$. If we consider a mirror of 100 mm focal length and 50 mm diameter, $T \approx 5$ ps.

In general, in the case where $F \ll \bar{\rho}$ (i.e., short distances and/or large emitting surfaces), the time T is so large that it effectively becomes infinite, removing the backtraveling peak from the measurements. In the opposite limiting case, when we have $F \gg \bar{\rho}$ (i.e., large distances or small emitting surfaces), the time T becomes short so that effectively the difference $\mathbf{J}(t) - \mathbf{J}(t-T)$ becomes proportional to the time derivative, thus again obtaining the original $\partial\mathbf{J}/\partial t$ from Jefimenko's equation.

2. Off-axis mirror

The case of a centered mirror described in the previous section was analytically straightforward, but adopted a somewhat simplifying approximation. In such a setup the detector would screen the mirror from the incident radiation (which we suppose directed parallel to the mirror symmetry axis), and hence off-axis mirrors need to be used.

As Fig. 5 shows, an off-axis mirror consists of a circular section cut out of a parabolic mirror (parent mirror) that focuses the reflected radiation towards the focus of the original parabola from which the mirror is cut. Relevant quantities in an off-axis parabolic mirror are:

(a) the radius R of the circumference that defines the circular section;

(b) the center of the mirror, that is, the center of the circular section—we choose a coordinate system so that the center is at the point $(x_0, 0, z_0)$;

(c) the effective focal length of the mirror, which is the distance between the center of the off-axis mirror and the focus of the original parabola;

(d) the focal length F of the parent mirror;

(e) the angle between the optical axis of the parent mirror and the line connecting the focal point of the parent mirror with the center of the off-axis mirror.

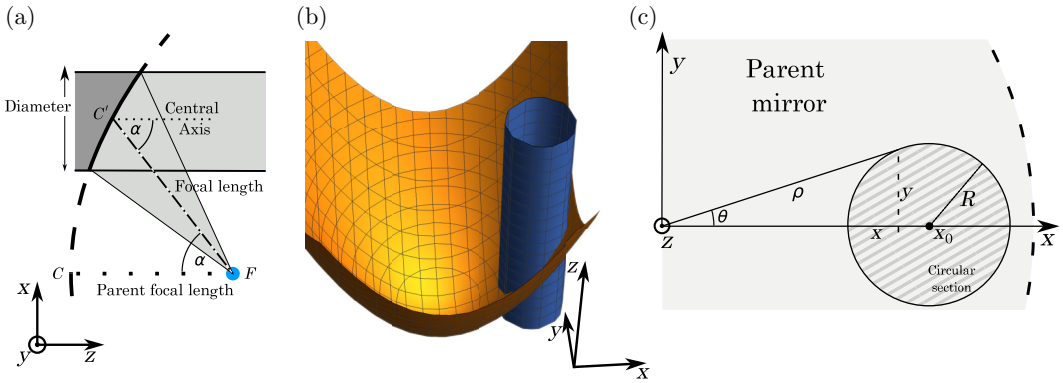

FIG. 5. Off-axis mirror as a section of a parabolic mirror. (a) Schematics of an off-axis mirror in the x-z plane; α is the off-axis angle. (b) Three-dimensional view of the circular section of a parabolic mirror. (c) Schematics of the circular section in the x-y plane.

As per Fig. 5(c), we consider here a 45° off-axis mirror, with a radius R of 25 mm and focal length of 100 mm. We choose a coordinate system where the parent parabolic mirror of parent focal length F is centered in the origin of the system; F can be computed knowing the coordinates of the off-axis mirror and its focal length. The center of the off-axis mirror is located at position x_0 on the x axis of the system.

The situation is less symmetric than in the previous case. The integral over the surface of the mirror has a different parametrization,

$$\mathbf{E}(\mathbf{r},t) \approx \frac{1}{r}\int_{x_0-R}^{x_0+R} dx \int_{-\sqrt{R^2-(x_0-x)^2}}^{\sqrt{R^2-(x_0-x)^2}} dy \times \frac{\partial \mathbf{J}}{\partial t}\left[t-\frac{1}{c}\left(F+\frac{x^2+y^2}{4F}\right)\right]. \tag{B7}$$

We can use polar coordinates as in the previous case, giving

$$\mathbf{E}(t) \approx \int_{\rho_1}^{\rho_2} \rho\, d\rho \int_{\theta_1}^{\theta_2} d\theta \frac{\partial \mathbf{J}}{\partial t}\left[t-\frac{1}{c}\left(F+\frac{\rho^2}{4F}\right)\right], \tag{B8}$$

where, for the sake of simplicity, we dropped the dependence on $\mathbf{r}$ in $\mathbf{E}$. The integration limits for the surface integral are $\rho_{1/2} = x_0 \mp R$ and

$$\theta_{1/2} = \mp \arctan\left(\sqrt{\frac{4x_0^2\rho^2}{(\rho^2+x_0^2-R^2)^2}-1}\right), \tag{B9}$$

and, after we integrate over θ,

$$\mathbf{E}(t) \approx \int_{x_0-R}^{x_0+R} \rho\, d\rho\; 2\arctan\left(\sqrt{\frac{4x_0^2\rho^2}{(\rho^2+x_0^2-R^2)^2}-1}\right) \times \frac{\partial \mathbf{J}}{\partial t}\left[t-\frac{1}{c}\left(F+\frac{\rho^2}{4F}\right)\right]. \tag{B10}$$

Next, we integrate by parts over ρ and take into account that

$$\frac{\partial \mathbf{J}}{\partial t} = \frac{\partial \mathbf{J}}{\partial \rho}\frac{\partial \rho}{\partial t} \quad \text{and} \quad \frac{\partial \rho}{\partial t} = -\frac{1}{\rho}2Fc. \tag{B11}$$

We can then rewrite Eq. (B10) as

$$-4Fc\int_{x_0-R}^{x_0+R} d\rho\, \arctan\left(\cdots\right)\frac{\partial \mathbf{J}[\cdots]}{\partial \rho} = -4Fc\, \arctan\left(\cdots\right)\mathbf{J}[\cdots]\Big|_{x_0-R}^{x_0+R} + 4Fc\int_{x_0-R}^{x_0+R} d\rho \frac{\partial}{\partial \rho}\arctan\left(\cdots\right)\mathbf{J}[\cdots], \tag{B12}$$

where we omitted the arguments of arctan and of $\mathbf{J}$ for the sake of brevity. The first term on the right-hand side is zero because the argument of the arctan is null at the integral boundaries. On the other hand, the derivative in the second term can be written explicitly as

$$\frac{\partial}{\partial \rho}\arctan\left(\sqrt{\frac{4x_0^2\rho^2}{(\rho^2+x_0^2-R^2)^2}-1}\right) = -\frac{R^2+\rho^2+x_0^2}{\rho\sqrt{4x_0^2\rho^2-(\rho^2+x_0^2-R^2)^2}}, \tag{B13}$$

so that

$$\mathbf{E}(t) \approx -4Fc\int_{x_0-R}^{x_0+R} d\rho\, \mathbf{J}\left[t-\frac{1}{c}\left(F+\frac{\rho^2}{4F}\right)\right]\frac{R^2+\rho^2+x_0^2}{\rho\sqrt{4x_0^2\rho^2-(\rho^2+x_0^2-R^2)^2}}. \tag{B14}$$

In this integral, $\mathbf{J}$ is multiplied by a function that is strongly peaked around the integral boundaries and low-valued everywhere else, as shown in Fig. 6. This means that the we can approximate the integral as $\mathbf{J}$ evaluated only at the peaks.

Finally, the result of the integral can be written as a linear combination of $\mathbf{J}$ evaluated at the peaks (the boundaries of the integral), giving

$$\mathbf{E}(t) \approx a\,\mathbf{J}\left[t-\frac{1}{c}\left(F+\frac{(x_0+R)^2}{4F}\right)\right] + b\,\mathbf{J}\left[t-\frac{1}{c}\left(F+\frac{(x_0-R)^2}{4F}\right)\right], \tag{B15}$$

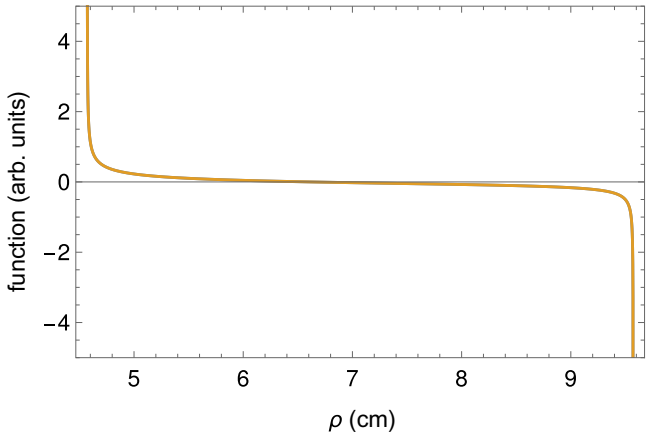

FIG. 6. Multiplying factor in the integral. The factor by which **J** is multiplied in Eq. (B14) is plotted in the integrating interval, $x_0 \pm x_R$, with $x_0 \approx 7.1$ cm. The function is divergent at the integral boundaries and almost flat and vanishing in the interval.

with

$$\frac{a}{b} = -\frac{4x_0(x_0+R)-1}{4x_0(x_0-R)-1}, \tag{B16}$$

which is negative and greater than 1 in modulus, meaning that the two peaks are opposite in sign, as in the previous case with the centered mirror. However, here the two peaks have different values, which is consistent with the less symmetric geometry of the mirror.

The time separation between the two peaks is $T = x_0R/(Fc)$, which is approximately 20 ps in the 15° case and 70 ps in the 45° case. Compared with the centered mirror case the separation of the two peaks is much larger, again due to the lower symmetry of this system. Furthermore, as we stated for the centered mirror case, after integrating over the surface of the mirror, the electric field becomes proportional to the charge-current density **J**.

As a last remark, we point out that the factor multiplying **J** in Eq. (B14) in the integral has, in contrast to, for example, a Dirac δ-function, peaks of finite width, meaning that after the integration the profile of **J** will be slightly distorted, as can be seen in Fig. 3.

APPENDIX C: RESPONSE FUNCTION OF THE DETECTOR CRYSTAL

In this section we summarize the theory of THz radiation detection through electro-optic crystals [47–49]. Specifically, we compute the response function of the detecting crystals used in THz experiments.

The detection of a THz pulse in a crystal is performed by propagating collinearly both the THz pulse and a probe pulse in the crystal. We consider here the case where the 800-nm pulse that excites the THz emission is split to be used as a probe pulse as well. As the THz pulse propagates in the crystal, it induces birefringence in it, which affects the propagation of the optical probe pulse. When both pulses propagate in the crystal, the polarization of the optical pulse rotates. By tracking the rotation of the polarization of the probe pulse the THz signal is reconstructed.

TABLE I. Model parameters for the electro-optical response of ZnTe crystals. The values given are taken from Ref. [48].

	ϵ_{el}	S_0	$\omega_0/2\pi$ [THz]	$\Lambda_0/2\pi$ [THz]	d_E [m/V]	C
ZnTe	7.4	2.7	5.35	0.09	$4.25\ 10^{-12}$	−0.07

To model the response of the crystal to the presence of the THz and probe pulses, we need to know the crystal optical properties, that is, we need information about the crystal refractive index and extinction coefficient. We model the dielectric constant of the crystal with the Lorentz oscillator model,

$$\epsilon(\omega) = \epsilon_{el} + \frac{S_0\omega_0^2}{\omega_0^2 - \omega^2 - i\Lambda_0\omega}. \tag{C1}$$

Here, the first term ϵ_{el} represents the contribution to the dielectric constant of bound electrons; it is constant in the THz range. The second term is the contribution from the lowest transverse-optical lattice oscillation in the crystal, treated as a damped harmonic oscillator (contributions from higher-order modes have been neglected). S_0 is the strength of the oscillator, ω_0 its eigenfrequency and Λ_0 the damping constant. The parameters for the ZnTe crystal that is commonly used in these experiments are reported in Table I. The refractive index of the crystal n and its extinction coefficient κ are, respectively, the real and imaginary part of $\epsilon^{1/2}$.

The refractive index of the crystal is frequency dependent. Because of this, the THz and probe pulse propagate through the crystal with different velocities. Therefore, the two pulses experience a phase mismatch (for convenience, the following quantities are expressed in terms of the frequency $f = \omega/2\pi$)

$$\Delta k(f) = \frac{2\pi f}{c}\left(n(f) - n_g(f_{\text{probe}})\right), \tag{C2}$$

where n_g represents the refracting index experienced by the probe signal in the crystal. The optical probe pulse travels with group velocity

$$v_g(f) = \frac{c}{n(f) + fn'(f)}, \tag{C3}$$

from which we can define the group refractive index as $n_g = c/v_g$, where c is the speed of light.

It follows that, as the two pulses propagate through a crystal with thickness d, the mismatch between the two increases, limiting the frequency window in which the probe pulse and the THz pulse can interact. By integrating the phase mismatch over the thickness of the crystal, we obtain the *geometric* response function of the crystal,

$$G(f) = \frac{1}{d}\int_0^d dz \exp\left(i\Delta k(f)z - \frac{2\pi f}{c}\kappa z\right). \quad \text{(C4)}$$

However, to obtain the electro-optical response function of the crystal, we must also take into account the frequency-dependent transmission properties of the crystal, summarized by the Fresnel transmission coefficient

$$T(f) = \frac{2}{1 + n(f) + i\kappa(f)}. \quad \text{(C5)}$$

Finally, merging the geometric response function and the transmission coefficient, we can define the electro-optical response function as

$$S_{\mathrm{EO}}(f) \approx r_{41}(f)G(f)T(f), \quad \text{(C6)}$$

where r_{41} is the electro-optical coefficient. This coefficient represents the shift in the refractive index of a medium when an electric field is applied to it. It can be modeled similarly with Lorentz oscillators as the dielectric function,

$$r_{41}(\omega) = d_E\left(1 + \frac{C\omega_0^2}{\omega_0^2 - \omega^2 - i\Lambda_0\omega}\right), \quad \text{(C7)}$$

where $r_{41}(f) = r_{41}(\omega/2\pi)$ and d_E and C are empirically determined coefficients and are reported in Table I.

Figure 7 shows the response function for a ZnTe crystal computed with Eq. (C6) and the parameters from Table I for different values of the crystal thickness d, normalized for easier visualization to the value of the response at zero frequency. We observe that the bandwidth of the detector quickly decreases with the thickness of the crystal. Moreover, the response shows oscillations and a resonance peak around the value $\omega_0/2\pi$, the frequency of the lowest transverse-optical lattice oscillation. This resonance peak is still present in the real response function; however, it should be less pronounced as the contributions of higher-order lattice oscillations mitigate the divergent behavior at ω_0.

Finally, we point out that the value of $n_g(f_{\mathrm{probe}}) = 3.1$ that we used to compute the response function for ZnTe in Fig. 7 has been increased by about 10% with respect of the value obtained by using the reported parameters ($n_g^{\mathrm{ZnTe}} = 2.72$), as this appeared more compatible with experimental findings.

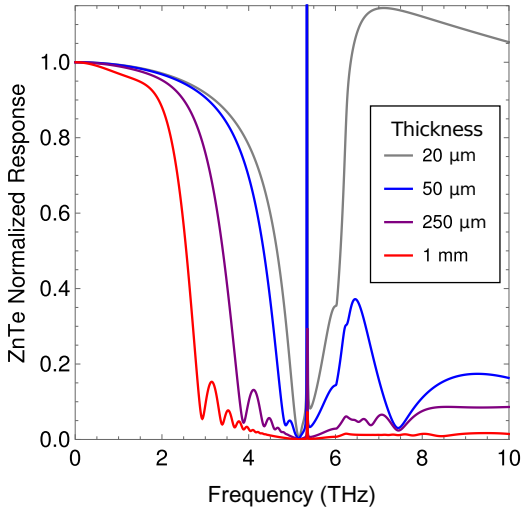

FIG. 7. ZnTe response function. The response function of the ZnTe crystal has been computed for different thicknesses of the detector crystal and for a wavelength of the probe pulse of 800 nm.

[1] B. Ferguson and X.-C. Zhang, Materials for terahertz science and technology, Nat. Mater. **1**, 26 (2002).
[2] M. Tonouchi, Cutting-edge terahertz technology, Nat. Photon. **1**, 97 (2007).
[3] Y.-S. Lee, *Principles of Terahertz Science and Technology* (Springer Science & Business Media, New York, 2009), Vol. 170.
[4] S. L. Dexheimer, *Terahertz Spectroscopy: Principles and Applications* (CRC Press, Boca Raton, 2017).
[5] D. M. Mittleman, Perspective: Terahertz science and technology, J. Appl. Phys. **122**, 230901 (2017).
[6] S.-C. Chen, Z. Feng, J. Li, W. Tan, L.-H. Du, J. Cai, Y. Ma, K. He, H. Ding, Z.-H. Zhai, Z.-R. Li, C.-W. Qiu, X.-C. Zhang, and L. Zhu, Ghost spintronic THz-emitter-array microscope, Light: Sci. Appl. **9**, 99 (2020).
[7] T. Seifert *et al.*, Efficient metallic spintronic emitters of ultrabroadband terahertz radiation, Nat. Photon. **10**, 483 (2016).
[8] S. S. Dhillon *et al.*, The 2017 terahertz science and technology roadmap, J. Phys. D: Appl. Phys. **50**, 043001 (2017).
[9] E. T. Papaioannou, G. Torosyan, S. Keller, L. Scheuer, M. Battiato, V. K. Mag-Usara, J. L'huillier, M. Tani, and R. Beigang, Efficient terahertz generation using Fe/Pt spintronic emitters pumped at different wavelengths, IEEE Trans. Magn. **54**, 1 (2018).
[10] M. Chen, Y. Wu, Y. Liu, K. Lee, X. Qiu, P. He, J. Yu, and H. Yang, Current-enhanced broadband THz emission from spintronic devices, Adv. Opt. Mater. **7**, 1801608 (2019).
[11] E. T. Papaioannou and R. Beigang, THz spintronic emitters: A review on achievements and future challenges, Nanophotonics **10**, 1243 (2020).
[12] A. Nahata, A. S. Weling, and T. F. Heinz, A wideband coherent terahertz spectroscopy system using optical

rectification and electro-optic sampling, Appl. Phys. Lett. **69**, 2321 (1996).
[13] N. M. Burford and M. O. El-Shenawee, Review of terahertz photoconductive antenna technology, Opt. Eng. **56**, 010901 (2017).
[14] T. Kampfrath, M. Battiato, P. Maldonado, G. Eilers, J. Nötzold, S. Mährlein, V. Zbarsky, F. Freimuth, Y. Mokrousov, S. Blügel, M. Wolf, I. Radu, P. M. Oppeneer, and M. Münzenberg, Terahertz spin current pulses controlled by magnetic heterostructures, Nat. Nanotechn. **8**, 256 (2013).
[15] Y. Wu, M. Elyasi, X. Qiu, M. Chen, Y. Liu, L. Ke, and H. Yang, High-performance THz emitters based on ferromagnetic/nonmagnetic heterostructures, Adv. Mater. **29**, 1603031 (2017).
[16] R. Adam, G. Chen, D. E. Bürgler, T. Shou, I. Komissarov, S. Heidtfeld, H. Hardtdegen, M. Mikulics, C. M. Schneider, and R. Sobolewski, Magnetically and optically tunable terahertz radiation from Ta/NiFe/Pt spintronic nanolayers generated by femtosecond laser pulses, Appl. Phys. Lett. **114**, 212405 (2019).
[17] T. H. Dang *et al.*, Ultrafast spin-currents and charge conversion at 3d-5d interfaces probed by time-domain terahertz spectroscopy, Appl. Phys. Rev. **7**, 041409 (2020).
[18] W. Wu, C. Yaw Ameyaw, M. F. Doty, and M. B. Jungfleisch, Principles of spintronic THz emitters, J. Appl. Phys. **130**, 091101 (2021).
[19] C. Bull, S. M. Hewett, R. Ji, C.-H. Lin, T. Thomson, D. M. Graham, and P. W. Nutter, Spintronic terahertz emitters: Status and prospects from a materials perspective, APL Mater. **9**, 090701 (2021).
[20] Z. Feng, H. Qiu, D. Wang, C. Zhang, S. Sun, B. Jin, and W. Tan, Spintronic terahertz emitter, J. Appl. Phys. **129**, 010901 (2021).
[21] P. Koleják, G. Lezier, D. Vala, B. Mathmann, L. Halagačka, Z. Gelnárová, Y. Dusch, J.-F. Lampin, N. Tiercelin, K. Postava, and M. Vanwolleghem, Maximizing the electromagnetic efficiency of spintronic terahertz emitters, Adv. Photon. Res. **5**, 2400064 (2024).
[22] A. Kefayati and B. K. Nikolić, Origins of electromagnetic radiation from spintronic terahertz emitters: A time-dependent density functional theory plus Jefimenko equations approach, Phys. Rev. Lett. **133**, 136704 (2024).
[23] M. Battiato, K. Carva, and P. M. Oppeneer, Superdiffusive spin transport as a mechanism of ultrafast demagnetization, Phys. Rev. Lett. **105**, 027203 (2010).
[24] M. Battiato, K. Carva, and P. M. Oppeneer, Theory of laser-induced ultrafast superdiffusive spin transport in layered heterostructures, Phys. Rev. B **86**, 024404 (2012).
[25] T. S. Seifert, N. M. Tran, O. Gueckstock, S. M. Rouzegar, L. Nadvornik, S. Jaiswal, G. Jakob, V. V. Temnov, M. Münzenberg, M. Wolf, M. Kläui, and T. Kampfrath, Terahertz spectroscopy for all-optical spintronic characterization of the spin-Hall-effect metals Pt, W and Cu80Ir20, J. Phys. D: Appl. Phys. **51**, 364003 (2018).
[26] G.-M. Choi, C.-H. Moon, B.-C. Min, K.-J. Lee, and D. G. Cahill, Thermal spin-transfer torque driven by the spin-dependent Seebeck effect in metallic spin-valves, Nat. Phys. **11**, 576 (2015).
[27] A. Alekhin, I. Razdolski, N. Ilin, J. P. Meyburg, D. Diesing, V. Roddatis, I. Rungger, M. Stamenova, S. Sanvito, U. Bovensiepen, and A. Melnikov, Femtosecond spin current pulses generated by the nonthermal spin-dependent Seebeck effect and interacting with ferromagnets in spin valves, Phys. Rev. Lett. **119**, 017202 (2017).
[28] M. Beens, R. A. Duine, and B. Koopmans, *s-d* model for local and nonlocal spin dynamics in laser-excited magnetic heterostructures, Phys. Rev. B **102**, 054442 (2020).
[29] T. Lichtenberg, M. Beens, M. H. Jansen, B. Koopmans, and R. A. Duine, Probing optically induced spin currents using terahertz spin waves in noncollinear magnetic bilayers, Phys. Rev. B **105**, 144416 (2022).
[30] T. J. Huisman, R. V. Mikhaylovskiy, A. Tsukamoto, T. Rasing, and A. V. Kimel, Simultaneous measurements of terahertz emission and magneto-optical Kerr effect for resolving ultrafast laser-induced demagnetization dynamics, Phys. Rev. B **92**, 104419 (2015).
[31] T. J. Huisman, R. V. Mikhaylovskiy, J. D. Costa, F. Freimuth, E. Paz, J. Ventura, P. P. Freitas, S. Blügel, Y. Mokrousov, T. Rasing, and A. V. Kimel, Femtosecond control of electric currents in metallic ferromagnetic heterostructures, Nat. Nanotechn. **11**, 455 (2016).
[32] D. M. Nenno, R. Binder, and H. C. Schneider, Simulation of hot-carrier dynamics and terahertz emission in laser-excited metallic bilayers, Phys. Rev. Appl. **11**, 054083 (2019).
[33] J. Pettine, P. Padmanabhan, N. Sirica, R. P. Prasankumar, A. J. Taylor, and H.-T. Chen, Ultrafast terahertz emission from emerging symmetry-broken materials, Light: Sci. Appl. **12**, 133 (2023).
[34] J. Varela-Manjarres, A. Kefayati, M. B. Jungfleisch, J. Q. Xiao, and B. K. Nikolić, Charge and spin current pumping by ultrafast demagnetization dynamics, Phys. Rev. B **110**, L060410 (2024).
[35] J. Gorchon, S. Mangin, M. Hehn, and G. Malinowski, Is terahertz emission a good probe of the spin current attenuation length?, Appl. Phys. Lett. **121**, 012402 (2022).
[36] O. D. Jefimenko, Solutions of Maxwell's equations for electric and magnetic fields in arbitrary media, Am. J. Phys. **60**, 899 (1992).
[37] H. Qiu, K. Kato, K. Hirota, and N. Sarukura, in *2018 43rd International Conference on Infrared, Millimeter, and Terahertz Waves (IRMMW-THz)* (IEEE, New York, 2018), p. 1.
[38] G. Li, R. Medapalli, R. V. Mikhaylovskiy, F. E. Spada, T. Rasing, E. E. Fullerton, and A. V. Kimel, THz emission from Co/Pt bilayers with varied roughness, crystal structure, and interface intermixing, Phys. Rev. Mater. **3**, 084415 (2019).
[39] P. Baláž, M. Zwierzycki, F. Cosco, K. Carva, P. Maldonado, and P. M. Oppeneer, Theory of superdiffusive spin transport in noncollinear magnetic multilayers, Phys. Rev. B **107**, 174418 (2023).
[40] A. E. Kaplan, Diffraction-induced transformation of near-cycle and subcycle pulses, J. Opt. Soc. Am. B **15**, 951 (1998).
[41] W.-T. Lu, Y. Zhao, M. Battiato, Y. Wu, and Z. Yuan, Interface reflectivity of a superdiffusive spin current in ultrafast demagnetization and terahertz emission, Phys. Rev. B **101**, 014435 (2020).
[42] V. P. Zhukov, E. V. Chulkov, and P. M. Echenique, Lifetimes and inelastic mean free path of low-energy excited

electrons in Fe, Ni, Pt, and Au: Ab initio GW+T calculations, Phys. Rev. B **73**, 125105 (2006).
[43] I. A. Nechaev and E. V. Chulkov, Quasiparticle dynamics in ferromagnetic compounds of the Co–Fe and Ni–Fe systems, Eur. Phys. Jour. B **77**, 31 (2010).
[44] M. I. Dyakonov and V. I. Perel, Current-induced spin orientation of electrons in semiconductors, Phys. Lett. A **35**, 459 (1971).
[45] J. E. Hirsch, Spin Hall effect, Phys. Rev. Lett. **83**, 1834 (1999).
[46] L. Salemi and P. M. Oppeneer, First-principles theory of intrinsic spin and orbital Hall and Nernst effects in metallic monoatomic crystals, Phys. Rev. Mater. **6**, 095001 (2022).
[47] B. Wu, L. Cao, Q. Fu, P. Tan, and Y. Xiong, in *Proceedings of the 5th International Particle Accelerator Conference* (JacoW Publishing, Geneva, 2014), p. 2891.
[48] S. Casalbuoni, H. Schlarb, B. Schmidt, P. Schmüser, B. Steffen, and A. Winter, Numerical studies on the electro-optic detection of femtosecond electron bunches, Phys. Rev. Special Topics—Accelerators and Beams **11**, 072802 (2008).
[49] G. Gallot and D. Grischkowsky, Electro-optic detection of terahertz radiation, J. Opt. Soc. Am. B **16**, 1204 (1999).
[50] E. Beaurepaire, G. M. Turner, S. M. Harrel, M. C. Beard, J.-Y. Bigot, and C. A. Schmuttenmaer, Coherent terahertz emission from ferromagnetic films excited by femtosecond laser pulses, Appl. Phys. Lett. **84**, 3465 (2004).
[51] W. Zhang, P. Maldonado, Z. Jin, T. S. Seifert, J. Arabski, G. Schmerber, E. Beaurepaire, M. Bonn, T. Kampfrath, P. M. Oppeneer, and D. Turchinovich, Ultrafast terahertz magnetometry, Nat. Commun. **11**, 4247 (2020).
[52] M. B. Jungfleisch, Q. Zhang, W. Zhang, J. E. Pearson, R. D. Schaller, H. Wen, and A. Hoffmann, Control of terahertz emission by ultrafast spin-charge current conversion at Rashba interfaces, Phys. Rev. Lett. **120**, 207207 (2018).
[53] C. Zhou, Y. P. Liu, Z. Wang, S. J. Ma, M. W. Jia, R. Q. Wu, L. Zhou, W. Zhang, M. K. Liu, Y. Z. Wu, and J. Qi, Broadband Terahertz generation via the interface inverse Rashba-Edelstein effect, Phys. Rev. Lett. **121**, 086801 (2018).
[54] E. Rongione, L. Baringthon, D. She, G. Patriarche, R. Lebrun, A. Lemaître, M. Morassi, N. Reyren, M. Mičica, J. Mangeney, J. Tignon, F. Bertran, S. Dhillon, P. Le Févre, H. Jaffrès, and J.-M. George, Spin-momentum locking and ultrafast spin-charge conversion in ultrathin epitaxial $Bi_{1-x}Sb_x$ topological insulator, Adv. Sci. **10**, 2301124 (2023).
[55] A. Melnikov, I. Razdolski, T. O. Wehling, E. T. Papaioannou, V. Roddatis, P. Fumagalli, O. Aktsipetrov, A. I. Lichtenstein, and U. Bovensiepen, Ultrafast transport of laser-excited spin-polarized carriers in Au/Fe/MgO(001), Phys. Rev. Lett. **107**, 076601 (2011).
[56] D. Rudolf, C. La-O-Vorakiat, M. Battiato, R. Adam, J. M. Shaw, E. Turgut, P. Maldonado, S. Mathias, P. Grychtol, H. T. Nembach, T. J. Silva, M. Aeschlimann, H. C. Kapteyn, M. M. Murnane, C. M. Schneider, and P. M. Oppeneer, Ultrafast magnetization enhancement in metallic multilayers driven by superdiffusive spin current, Nat. Commun. **3**, 1037 (2012).
[57] M. Hofherr, P. Maldonado, O. Schmitt, M. Berritta, U. Bierbrauer, S. Sadashivaiah, A. J. Schellekens, B. Koopmans, D. Steil, M. Cinchetti, B. Stadtmüller, P. M. Oppeneer, S. Mathias, and M. Aeschlimann, Speed and efficiency of femtosecond spin current injection into a nonmagnetic material, Phys. Rev. B **96**, 100403 (2017).
[58] R. Gupta, F. Cosco, R. S. Malik, X. Chen, S. Saha, A. Ghosh, T. Pohlmann, J. R. L. Mardegan, S. Francoual, R. Stefanuik, J. Söderström, B. Sanyal, O. Karis, P. Svedlindh, P. M. Oppeneer, and R. Knut, Element-resolved evidence of superdiffusive spin current arising from ultrafast demagnetization process, Phys. Rev. B **108**, 064427 (2023).
[59] X. Wang, W. Sun, Y. Cui, J. Ye, S. Feng, and Y. Zhang, Complete presentation of the Gouy phase shift with the THz digital holography, Opt. Express **21**, 2337 (2013).
[60] A. B. Ruffin, J. V. Rudd, J. F. Whitaker, S. Feng, and H. G. Winful, Direct observation of the Gouy phase shift with single-cycle terahertz pulses, Phys. Rev. Lett. **83**, 3410 (1999).